

---

---



---

---

---

# Contents

<b>Table of Contents</b>	i
<b>List of Figures</b>	i
<b>List of Tables</b>	ii
<b>1 Silicon Vacancy Centers in Diamond</b>	1
1.1 Diamond as a host lattice . . . . .	1
1.2 Classification of diamond . . . . .	2
1.2.1 Classification by impurities . . . . .	2
1.2.2 Classification by crystallinity . . . . .	3
1.3 Silicon-vacancy center . . . . .	4
1.3.1 Luminescence properties . . . . .	5
<b>2 Fabrication of Nanodiamonds</b>	11
2.1 HPHT . . . . .	11
2.2 CVD . . . . .	12
2.3 Wet-Milling . . . . .	13
2.3.1 Wet-Milled HPHT Nanodiamonds . . . . .	15
2.3.2 Wet-Milled chemical vapor deposition Nanodiamonds . . . . .	15
2.3.3 Doubly Wet-Milled Implanted Nanodiamonds Implanted With Silicon .	17
2.4 Iridium Substrate . . . . .	19
2.4.1 Preparation of The Substrate . . . . .	20
<b>Bibliography</b>	21

---

---

# List of Figures

1.1	Face-centered cubic diamond lattice . . . . .	2
1.2	Reduced light extraction efficiency of diamond due to refraction . . . . .	2
1.3	Split-vacancy configuration for SiV centers in diamond . . . . .	5
1.4	Band gap of SiV centers hosted in diamond . . . . .	6
1.5	Huang-Rhys model of vibrational transitions . . . . .	8
1.6	Flourescence spectra of SiV centers at room temperature . . . . .	9
1.7	Flourescence spectra of SiV centers at low temperature . . . . .	10
2.1	SEM images of CVD grown diamonds (sample insitucvd) produced by M. Schreck's group (Augsburg University). The average size of these nanodiamonds is 100 nm. (a) Overview image, white dots are nanodiamonds. (b) Detail image, it can be seen that not all nanodiamonds exhibit the same size and that they coexist in different shapes. . . . .	12
2.2	Sketch showing the production of CVD nanodiamonds in the growth chamber with a methane gas environment. . . . .	12
2.3	Pictures of the milled nanodiamonds (sample insitu100). (a) SEM picture showing the distribution of the nanodiamond crystals on the iridium substrate ( <b>sample insitu100</b> ). (b) Sketch showing the wet-milling process in a vibrational mill. Vibrations from the mill drive the beads which collide with the diamond material and crush it to smaller pieces. . . . .	14
2.4	(a) SEM picture of nanodiamonds sunken into a silicon substrate after annealing at 900 °C for 3 h. Magnification 20 000. (b) SEM image of the microdiamonds after milling on an iridium substrate, but before implantation. In the middle of the picture, there is a reference cross milled into the iridium substrate with a focused ion beam. Its size amounts to 10 µm. It can be seen, that the microdiamonds exhibit sizes of a few micrometer. . . . .	16
2.5	(a) Microcope image of a drop of water on an iridium substrate cleaned with Piranha etch. This picture was used to estimate the contact angle. (b) SEM picture of an 60 nm iridium layer that peeled off the substrate after an ultrasonic bath. . . . .	19

---

---

# List of Tables

1.1	Classification of diamond synthesized by chemical vapor deposition . . . . .	4
2.1	Summary of the samples grown on diamondoid seed crystals. . . . .	14
2.2	Summary of the wet-milled samples. The first column indicates the names of the samples, the second the mean diameter of the nanodiamonds, and the third describes how the silicon was incorporated into the diamond. . . . .	18

---

---

# Chapter 1

# Silicon Vacancy Centers in Diamond

In the following we introduce color centers, i.e. optically active point-defects, present in a diamond lattice. We focus on color centers combining silicon impurities and lattice vacancies (SiV) in particular since their experimental study is at the focus of this thesis. We start by presenting the most important properties of diamond and emphasize its suitability as a host for optical applications with color centers. A classification of diamond with respects to defects and impurities as well as crystallinities serves as a preparation for the introduction of methods to synthesize diamonds containing SiV centers presented in ?? . Finally, we discuss SiV centers in detail and focus on their most important optical properties as reliable single-photon sources at room temperature. In particular, we zoom in on the key features of its luminescence spectrum, the zero-phonon-line and the phonon side band. Our discussion partially follows the presentation in [?, 1, ?, 2].

## 1.1 Diamond as a host lattice

Diamond is a metastable modification of carbon which is, in fact, stable under normal pressure and at room temperature [3]. Carbon atoms form strong  $sp^3$ -bonds with each other in a tetrahedral arrangement of neighboring atoms. The resulting  $sp^3$ -hybridized lattice is of exceptional mechanical stability, making diamond the hardest known material [?]. The crystal structure can also be interpreted as a face-centered cubic (fcc) lattice with two carbon atoms in the primitive Bravais cell, situated at  $(0, 0, 0)$   $a$  and  $(\frac{1}{4}, \frac{1}{4}, \frac{1}{4})$   $a$  with  $a = 3.567 \text{ \AA}$  denoting the lattice constant [4]. Figure 1.1 illustrates the structure.

The valence and conduction bands of diamond are separated energetically by a large direct band gap of 7.3 eV while its indirect band gap amounts to 5.5 eV [5, 6]. As a result diamonds are transparent for light of all wavelengths larger than 230 nm [7]. This transparent quality makes diamond an ideal host material for various optically active lattice defects or impurities. These induce a wide range of discrete energy levels accommodated by the sizable band gap. The absorption of optically active impurities or impurity complexes gives rise to the color of diamonds, thus these impurities are commonly termed color centers [1]. Due to the exceptional mechanical stability of diamond color centers too are very stable, another important property enabling optical applications.

A property of diamond, detrimental to some optical applications, is its large refractive index

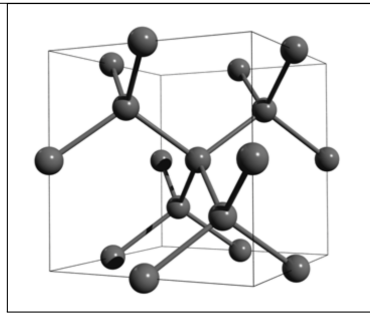


Figure 1.1: Face-centered cubic diamond lattice. Note the tetraedal arrangements of carbon atoms. Figure reproduced with permission from [?].

with values of 2.49 at 360 nm and 2.4 at 800 nm respectively [8]. Thus, a portion of the fluorescent light escaping from the diamond is reflected back into it, effectively reducing the efficiency of light extraction. If nanodiamonds smaller than the wavelength of the light to be collected are used, internal reflection is suppressed and the extraction efficiency can be increased [9].

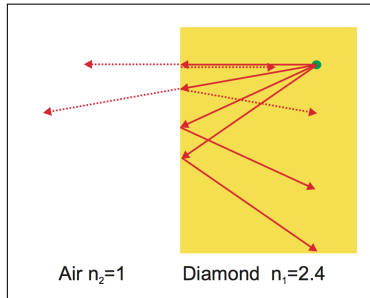


Figure 1.2: Light from a fluorescent emitter inside the diamond (green dot) undergoes reflection at the diamond-air interface. Figure reproduced with permission from [1].

## 1.2 Classification of diamond

Two major approaches for classifying diamond are commonly encountered. First, classification according to the presence or absence of certain impurities or impurity complexes. Second, classification based on different diamond crystallinities observed. In the following both classification systems are briefly introduced.

### 1.2.1 Classification by impurities

Impurities or complexes of impurities in the diamond lattice can be optically active and thus change the optical properties of diamond. Most strikingly perhaps is the appearance of color in otherwise colorless diamond due to a sufficient concentration of such defects. Using IR absorption spectroscopy the degree of nitrogen impurities can be determined. It is used to subdivide diamonds into distinct groups named Type I and Type II [?, ?]. The groups are further subdivided as follows:

- Type Ia: With a nitrogen concentration of up to 3000 ppm most natural occurring diamonds belong to this group [8]. Nitrogen appears arranged predominantly in aggregate clusters forming complexes of impurities. These complexes are optically active, absorbing light in the blue range of the visible spectrum. Consequently Type Ia diamonds often exhibit a yellow to brownish coloration.
- Type Ib: With concentrations of up to 500 ppm nitrogen atoms appear predominantly in isolation, replacing individual carbon atoms in the diamond lattice. In addition to absorbing visible blue light, green is being absorbed as well. Type Ib diamond thus exhibits intensified the yellow or brownish coloration. While only 0.1% of naturally occurring diamond fall into this class, almost all synthetic diamonds created using the high-pressure, high-temperature (HPHT) method are of Type Ib [8].

While Type I diamond exhibits an appreciable concentration of nitrogen, Type II diamonds lack nitrogen entirely. Type II diamond is divided into two subgroups according to the presence or absence of boron as follows:

- Type IIa: Can be considered pure as they lack boron impurities and other optically active defects [10]. They thus are colorless. Up to 2% of naturally occurring diamond and most diamonds synthetically created using the chemical vapor deposition (CVD) method are of Type IIa [8].
- Type IIb: Contains appreciable concentrations of boron atoms replacing individual carbon atoms in the diamond lattice. Boron defects are optically active absorbing visible light ranging from red to yellow. Depending on the Boron concentration blue to grey colorations are observed. Furthermore, diamond is turned from an insulator to a efficient p-type semiconductor in the presence of boron impurities [11].

We remark that for many modern applications of diamonds the presented "classic" categorisation of diamond is not enough. In these cases a precise quantification of the concentration and nature of various relevant impurities is called for [12, 13].

In this section we also briefly touched upon the CVD and HPHT methods, two approaches to synthetically produce diamonds. Both are relevant for this thesis and are explained in detail in ?? .

### 1.2.2 Classification by crystallinity

Up until now, the discussion assumed that diamond forms a lattice consisting of one giant single crystal. However, other crystallinities are possible and can be used to classify diamond. They range from mono or single crystals to polycrystalline, nanocrystalline or even ultra-nanocrystalline diamond films [14]. This classification is particularly useful for synthesized diamond as will be discussed in ?? . Table 1.1 summarizes the different sizes of diamonds or diamond films which can be achieved using variations of the CVD method.

Diamond films consist of isolated diamond grain of random orientation with sp<sup>2</sup> hybridized grain boundaries and graphit-like inclusions [?]. Carbon present in non-diamond phases, e.g. graphite or amorphous carbon gives rise to detrimental light absorption while crystal boundaries lead to increased scattering losses. As the size of diamond crystallites get smaller, the

ratio of non-diamond carbon to diamond carbon increases. Thus losses are most pronounced for the smallest grain diamond films.

Table 1.1: Classification of diamonds synthesized using CVD [2].

Crystallinity	Grain size
monocrystalline	arbitrary
polycrystalline	50 nm to 10 $\mu\text{m}$
nanocrystalline	10 nm to 50 nm
ultra-nanocrystalline	< 10 nm

### 1.3 Silicon-vacancy center

A color center is an optically active point-defect in a crystal lattice, capable of absorbing and emitting light. Defects can consist of one or several vacant lattice sites, foreign atoms replacing lattice atoms or a combination thereof. If the presence of a defect induces discrete energy levels located in the band gap of the host material, the color center can be interpreted as its own quantum system. In other words, the color center can be viewed as a single isolated and localized artificial atom embedded in a host matrix. As such it is able to absorb light and emit single photons by means of fluorescence.

Compared to alternative single photon sources like single atoms [15], Ions [16] or individual quantum dots [17, 18], color centers offer a couple of advantages due to their solid state environment. As a result of the high mechanical stability of the host lattice color centers exhibit increased photo-stability, in particular compared to organic molecules as light sources. Furthermore the host lattices offers protection for color centers from detrimental interactions with aggressive free molecules [19]. Lastly, color centers can be handled and investigated at room temperature, thus significantly reducing the experimental efforts necessary to study them.

Of particular interest are color centers as single photon sources when hosted in diamond. With its transparency, exceptional stability and minimal phononic interactions at room temperature the diamond lattice is an ideal host matrix for color centers [20, ?]. While more than 500 different color centers in diamond are documented, only a small fraction has been investigated with respect to their properties as single photon sources [8]. For an in-depth review of color centers and their versatile applications see [?, ?]. The two arguably most prominent examples of well-studied color centers are vacancy centers featuring nitrogen and silicon [?, ?, ?].

The silicon-vacancy (SiV) center in diamond and its properties is at the center of this thesis. The SiV center has been established as an efficient single photon source at room temperature. It shows very narrow emission lines with record count rates up to  $6.2 \times 10^6$  cps (counts-per-second) [?]. The emission of indistinguishable photons and the optical access of electronic spin states have been demonstrated [?, ?, ?, ?], hinting at the possibility of deploying SiV centers as spin-qubits.

A silicon-vacancy center is formed in a diamond lattice by substituting two carbon atoms by a silicon atom and a nearby empty lattice site respectively. The silicon atom occupies its

energetically optimal position by sitting in-between two lattice sites. This is called “split-vacancy” configuration and induces a  $D_{3d}$  symmetry with the two vacancies and the impurity alligned along the  $\langle 111 \rangle$  diamond axis [?], see Figure 1.3.

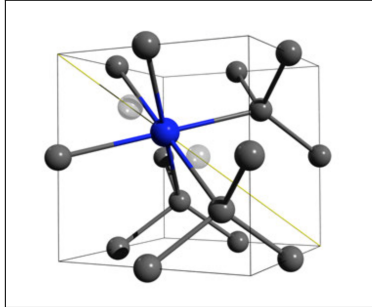


Figure 1.3: Crystal structure of the SiV center embedded into the diamond lattice: The silicon atom (blue sphere) sits in between two vacant lattice sites (white spheres) forming a “split-vacancy” configuration aligned along the  $\langle 111 \rangle$  crystallographic axis (yellow line). Figure reproduced with permission from [?].

The SiV center is known to occur in two different charge states. The first is the neutral state or  $\text{SiV}^0$  with a zero-phonon transition at 1.31 eV (946 nm). It is associated with a  $S = 1$  ground state [?]. The second state is the negatively charged state  $\text{SiV}^-$  where the silicon-vacancy center recruited an additional free electron. It exhibits a zero-phonon transition at 1.68 eV (738 nm). Its ground state has been determined as a  $S = \frac{1}{2}$  state [?, ?]. Due to its outstanding brightness and the location of the zero-phonon-line in the visible range of the spectrum, this thesis focuses on the negatively charged SiV center. For convenience we drop the charge distinction from now on and refer to  $\text{SiV}^-$  centers simply as SiV centers.

SiV centers have been created using CVD in nanodiamonds and single-crystal diamond films [?], see ?? for details. It is also possible to directly implant silicon atoms into pure diamond. High temperature annealing must then be used to animate present lattice vacancies to recombine with silicon impurities in order to form split-vacancy SiV centers [?, ?].

In the following sections we detail the most important luminescence properties of SiV centers in diamond. For a comprehensive review we refer to [?, 1] and references therein.

### 1.3.1 Luminescence properties

The silicon-vacancy center as a quasi-atomic system is capable of absorbing and emitting light. When a ground state electron absorbs a photon of appropriate energy, it is promoted to a discrete higher-energy excited state located within the band gap of the diamond host matrix. Reversing this excitation relaxes the electron back down to the ground state while emitting a so-called fluorescent photon, accounting for the energy difference between excited and ground state. This transition is “spin-allowed”, limiting the life-times of excited states to nano-seconds and thus promoting rapid relaxation and associated fluorescence [?].

Since fluorescence is directly linked to the electronic structure of the SiV center, see Figure 1.4. It follows that photoluminescence spectroscopy can be used to study it using a laser to optically excite the SiV center. In the context of this thesis, optical above-resonant excitation is

the method of choice, in particular, when used in conjunction with a confocal photoluminescence setup which will be discussed in [??](#). If the excitation energy exceeds the energy of the lowest excited state, electrons are promoted to higher electronic and vibrational states. Conveniently, these states relax rapidly towards the lowest excited state in non-radiative processes [\[?\]](#). Once the lowest excited state is reached, a fluorescent transition can follow. It has been shown that above-resonant excitation is feasible for excitation energies ranging from 1.75 eV to 2.55 eV [\[?, 21, 22\]](#). If the excitation energy is chosen too high, however, the SiV center is ionized. Electrons donated to the diamond conduction band do not participate in fluorescence. Ionization may be reversed if a positively charged SiV center manages to capture a free electron from the conduction band. This charge state conversion is believed to be linked to fluorescence intermittence, more intuitively named as blinking SiV centers [\[23, 24\]](#).

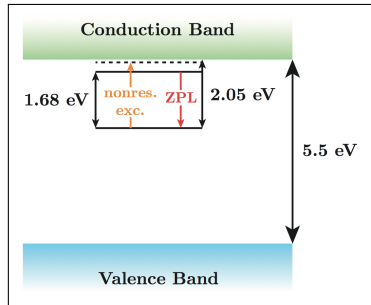


Figure 1.4: Simplified picture of the generous 5.5 eV band gap of diamond with discrete states induced by the presence of SiV centers. The SiV center ground state is situated 2.05 eV below the diamond conduction band. The lowest excited state sits 1.68 eV above the ground state with the zero-phonon-line transition in red connecting the two. Above-resonant optical excitation is indicated in orange. Figure courtesy of [\[?\]](#).

The fluorescence spectrum of SiV centers have two prominent features: A narrow zero-phonon-line and a broad phonon side band. The former is connected to fluorescent photons associated with a purely electronic transition while the latter involves vibrational transitions involving electron-phonon interactions. The phonon side band is typically shifted to higher wavelengths with respect to the zero-phonon-line. The resulting energy deficit can be explained by phonons being created during the relaxation of higher vibrational states. A shift in the opposite direction can also be observed in rare cases if phonons are absorbed during the relaxation process [\[?\]](#).

The relative strength of the zero-phonon-line and the phonon side band is connected to the electron-phonon coupling of the excited color center and thus to lattice vibrations. When a color center is excited, its charge distribution changes. As a result, the equilibrium positions of all particles involved in the color center shift leading to changes in color center geometry. Naturally, the combined changes of charge distribution and geometry of the color center affect the surrounding atoms of the host lattice. Similarly, if the excited state relaxes back to the ground state, the process occurs in reverse. Thus, due to differing atomic arrangements for ground and excited states, the emission and absorption of photons is accompanied by lattice vibrations, i.e. phonons. In other words, the electron-phonon interaction couples the motion of the lattice and electronic transitions of a color center [\[25, 26\]](#).

The Huang-Rhys model allows us to discuss the electron-phonon interaction in SiV centers in more detail. Our discussion follows the presentation in [\[?\]](#). The model assumes in its

simplest form that vibrational modes can be modelled as oscillations of nuclei between their equilibrium coordinates  $q$  associated with the electronic states [?]. Let  $\mathcal{K}_{^3A_2}(q)$  and  $\mathcal{K}_{^3E}(q)$  denote the harmonic potentials of the ground and excited states respectively:

$$\mathcal{K}_{^3A_2}(q) = \frac{1}{2}\Omega^2 q^2 \quad (1.1)$$

$$\mathcal{K}_{^3E}(q) = C_{^3E} + aq + \frac{1}{2}(\Omega^2 + b)q^2 \quad (1.2)$$

$$= C_{^3E} - C_R + \frac{1}{2}(\Omega^2 + b)(q - \delta q)^2. \quad (1.3)$$

It follows that the vibrational modes of ground and excited states are given as harmonic states with discrete energies  $\hbar\Omega(\nu + 2)$  as well as  $\hbar\sqrt{\Omega + b}(\nu + 2)$  respectively, where  $\nu$  denotes the occupation number and  $\Omega$  the frequency. Further, let  $aq$  denote the linear nuclear displacement of the excited state configuration with respect to the ground state equilibrium where  $q = 0$  holds. The quadratic term  $bq^2$  refers to the vibrational frequency shift due to a redistribution of charge between the electronic states. Given the linear and quadratic electron-phonon coupling strengths  $a$  and  $b$ , the equilibrium displacement of the  ${}^3E$  state can be obtained as:

$$\delta q = \frac{-a}{\Omega^2 + b}, \quad (1.4)$$

while the relaxation energy reads [?]:

$$C_R = \frac{a^2}{2(\Omega^2 + b)} = \hbar S \sqrt{\Omega + b}, \quad (1.5)$$

where  $S$  is referred to as Huang-Rhys factor.

To reason about the probabilities of various transitions between different vibrational levels associated with ground and excited states, the Franck-Condon principle can be applied [?, ?]. It states that transitions between electronic states become more probable if origin and destination states have vibrational levels with similar energy. This implies that the most probable transitions occur between states requiring no change of nuclei positions. Figure 1.5 illustrates the application of the principle for the Huang-Rhys model.

We find that the most probable optical relaxation from an  ${}^3E$  excited state back to an  ${}^3A_2$  ground state originates from the fundamental vibrational  ${}^3E$  state, i.e. the lowest-energy excited state. This state is shifted by  $\delta q$  with respect to the ground state, indicating that the energetically optimal nuclei positions differ from their ground state equilibrium positions. The most probable destination of the relaxation is a higher vibrational level of the  ${}^3A_2$  ground state with similar nuclei positions. From there, electron-phonon interactions continue the relaxation process down to the fundamental vibrational level of the ground state. This non-radiative process allows nuclei to return to their original ground state equilibrium positions. The process of exciting the system from the ground state, proceeds in reverse. The most probable optical excitation promotes an electron from the fundamental  ${}^3A_2$  ground state to a higher vibrational level of the  ${}^3E$  excited state. The optical transition is such that nuclei positions do not change. Note that optical transitions are faster than vibrational transitions

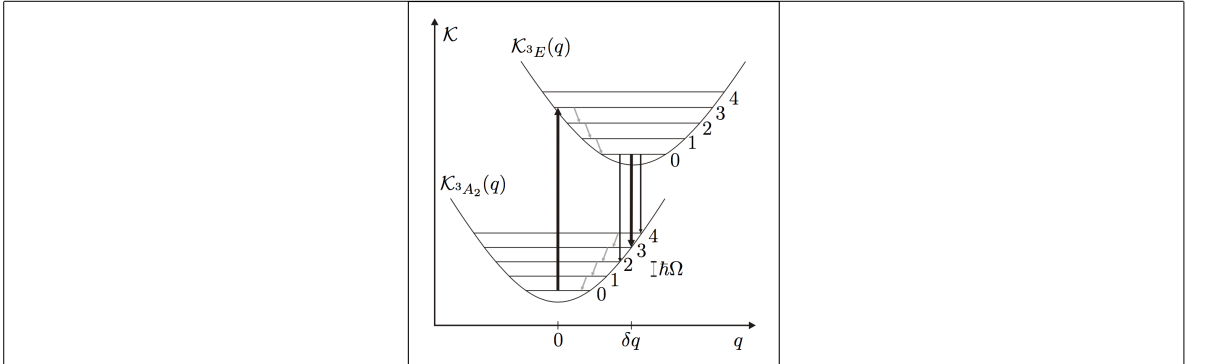


Figure 1.5: Huang-Rhys model of the vibrational transitions in the Frank-Condon picture: The excited state  $\mathcal{K}_{3E}(q)$  is shifted by  $\delta q$  with respect to the ground state potential  $\mathcal{K}_{3A_2}(q)$ . The recombination originating at  $\delta q$  marks the most probable transition (thick black arrow) from the fundamental  $^3E$  vibrational level to one of the vibrational levels of the  $^3A_2$  ground state followed by non-radiative transitions to the equilibrium position  $q = 0$ . The number of vibrational quanta involved in an optical transition are determined by the Huang-Rhys factor  $S$ . The excitation reverses the process. Optical transitions occur between states with identical values of  $q$  and are shown as vertical black arrows. Non-radiative transitions change the value of  $q$  and are shown as angled gray arrows. Figure and caption reproduced with permission [?].

since they do not require a change in nuclei positions. Once in the higher vibrational excited state, electron-phonon interactions mediate a transition down to the fundamental  $^3E$  excited state with an associated change in nuclei positions. From there the relaxation-excitation cycle and its induced periodic changes in nuclei positions repeats.

As discussed, transitions involving phonons mostly originate from the fundamental vibrational level of excited electronic states and end in higher vibrational states of the electronic ground state. Photons emitted during the relaxation process are associated with the phonon side band of the SiV center. The observed red-shift of the phonon side band is directly tied to the phonon energy with higher order sidebands showing multiples of this energy. Note that the The Huang-Rhys factor  $S$  can be interpreted as an indicator of the most probable optical transition involving photons. Thus, it can be used to quantify the strength of the electron-phonon interactions in SiV centers. A small value of  $S$  indicates a weak electron-phonon coupling resulting in negligible phonon side band emmisions. If no phonons are involved, the entire emission is concentrated in the zero-phonon-line. Conversely, a large value of  $S$  indicates extensive electron-phonon interactions, leading to a pronounced phonon side band and a weaker zero-phonon-line. This dependence is naturally described by

$$\frac{I_{ZPL}}{I_{ZPL} + I_{PSB}} \quad (1.6)$$

For SiV centers hosted in polycrystalline diamonds the Huang-Rhys factors have been determined to be very small ranging from 0.08 to 0.24 [27, 18, 28]. As a result the zero-phonon-line as the most probable transition dominates the luminescence spectrum making SiV centers excellent narrow-band emitters. Figure 1.6 illustrates the stark difference between the zero-phonon-line and the phonon side band. In contrast,  $S = 3.74$  has been established for nitrogen

vacancy centers [25]. A electron-phonon coupling of this magnitude concentrates almost all emission into the phonon side band and leaves the zero-phonon-line almost indetectable.

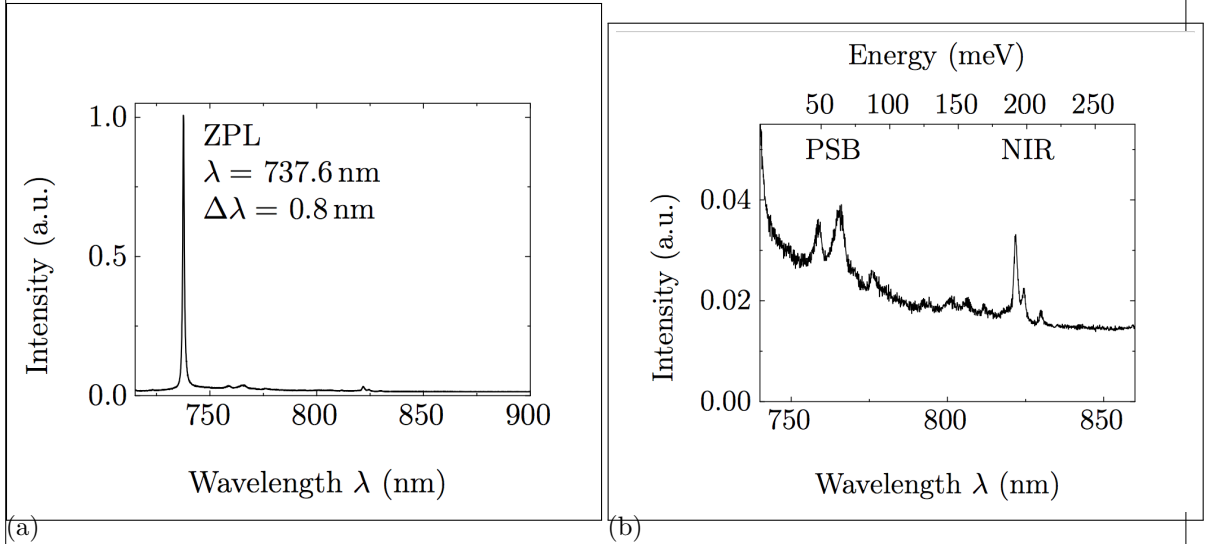


Figure 1.6: (a) The narrow zero-phonon-line dominates the luminescence spectrum. (b) Low intensity phonon side band shows distinct vibrational transitions. Figure reproduced with permission [?].

As an alternative measure for the electron-phonon coupling the Debeye-Waller factor can be used. It is closely related to the Huang-Rhys factor and defined as

$$D_w = e^{-S}, \quad (1.7)$$

which can be interpreted as the fraction of total photons that are emitted into the zero-phonon-line.

We remark at this point, that our discussion based on the Huang-Rhys model is assumes that only one vibrational mode couples to the color center which is a strong assumption. In general it is believed that in a solid state host matrix a discrimination between the modes of the undisturbed lattice and quasi-local impurity-induced modes is appropriate [26, 29, 30]. Furthermore, various mechanical properties such as stress in the lattice are reported to affect phonon energies [31]. In addition electron-phonon interactions and thus phonon side band features are believed to depend strongly on various local properties of color centers [32, 33]. Thus it is possible to encounter varying phonon side band features from one SiV center to the next. For a more detailed discussion of these effects we refer the reader to [1, ?] and references therein.

We close this chapter with a short discussion of the luminescence spectra of SiV centers at cryogenic temperatures. Naturally as temperatures approach absolute-zero the phonon side band must disappear. If SiV centers are cooled below  $\approx 110 \text{ K}$  a fine structure is revealed [?]. It includes up to 12 different lines with intensities proportional to the natural abundance of the three stable isotopes of silicon  $^{28}\text{Si}$ ,  $^{29}\text{Si}$ ,  $^{30}\text{Si}$  [?]. Each isotope is associated with 4 lines attributed to doublet levels of ground and excited states which are split by 0.2 meV and 1.07 meV respectively [?, ?, ?]. The splitting itself is believed to be a result of spin-orbit

coupling with a weak contribution of the dynamic Jahn-Teller effect [?]. Initial results were based on ensembles of SiV centers, however, recently the splitting was detected for isolated SiV centers as well [?]. Figure 1.7 shows exemplary spectra representative for ensembles and single SiV center at cryogenic temperatures.

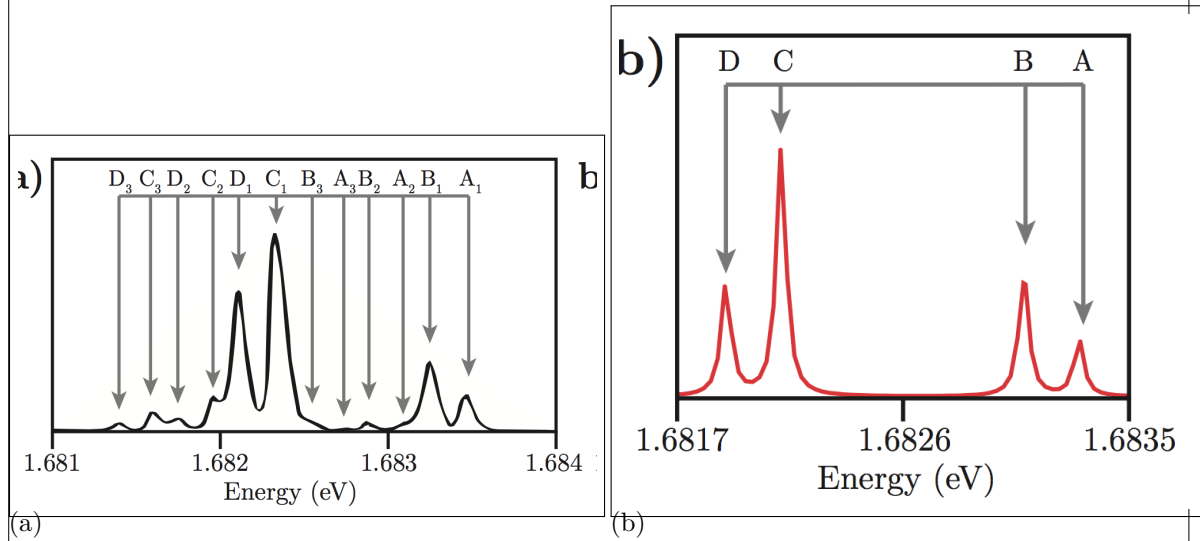


Figure 1.7: (a) Fluorescence spectrum of an ensemble of SiV centers at 10 K. 12 peaks can be seen, 4 for each stable isotope of silicon [?]. (b) Fluorescence spectrum of an isolated SiV center at 15 K. 4 peaks can be seen, 2 for the ground state and 2 for the excited state. Figure reproduced from [?].

---

---

## Chapter 2

# Fabrication of Nanodiamonds

“Diamond forms under high temperature and pressure conditions that exist only about 100 miles beneath the earth’s surface.” (Homepage of the Gemological Institute of America Inc.) While this statement is true for natural gem diamonds, various methods exist to synthetically produce diamond for applications in industry and research. In this chapter, different fabrication methods of diamonds and nanodiamonds in particular are explained. The first two procedures described are the high-pressure, high-temperature method and the chemical vapor deposition are described. These are two of the most commonly used fabrication methods for laboratory-produced diamonds. The high-pressure, high-temperature (HPHT) process mimics natural conditions under which diamond is formed within earth and is widely used to synthetically produce diamonds for industry. While these HPHT diamonds are exploited for some experiments reported in this work, most measurements which are subject in this thesis are carried out on diamond produced with a CVD process. The third method which is described is the wet-milling process in a vibrational mill, which is a technique using chemical vapor deposition or HPHT diamond. Nanodiamonds produced with this milling process are the main focus of this thesis. It has to be stressed, that in contrast to the first two methods described in this chapter, the wet-milling process is not a process to produce diamond itself, rather it serves to crush bigger diamond starting material into pieces of a desired size. For a more extensive list of diamond production processes refer to e.g. [34]. Aside from the general diamond fabrication processes, the production details of the nanodiamonds used for this thesis will be mentioned.

### 2.1 High-Pressure High-Temperature Diamond

The HPHT process was the first process to successfully synthesize diamond (in 1879). Temperatures of a few thousand degrees Celsius and pressures between 50 000 bar and 100 000 bar are needed [34]. Today, it is still widely used due to its relatively cheap production costs [35]. In the HPHT process, diamond is synthesized from graphite. The machine used for this kind of synthesis is a press. For some forms of this method, a metallic solvent is added which lowers the needed pressures; the solvent causes the graphite to dissolve at lower pressures and temperatures, and at the same time it causes the diamond to crystallize. Several press designs exist, which all provide a high temperature and a high pressure in their core. While it is possible to grow big ( $> 10$  carat) high-quality diamonds with the HPHT process, it is

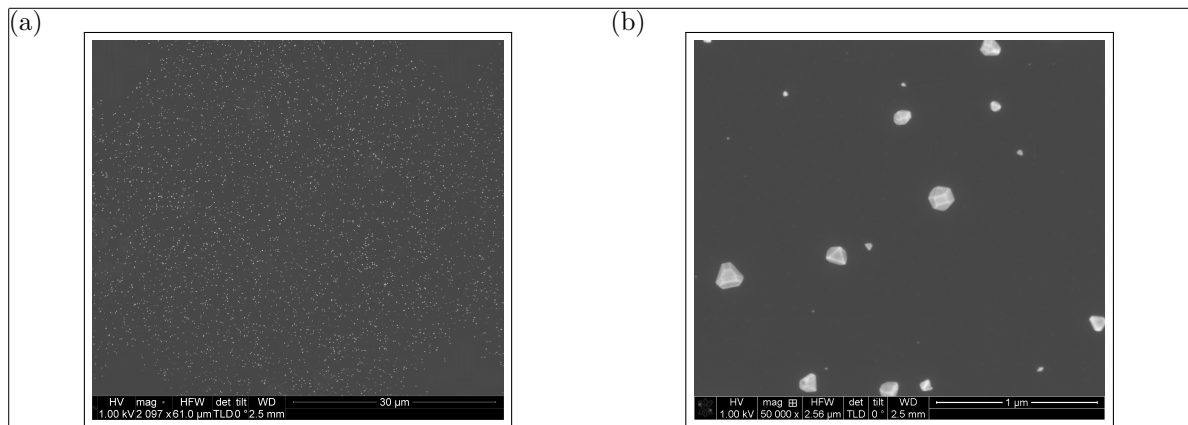


Figure 2.1: SEM images of CVD grown diamonds (sample insitucvd) produced by M. Schreck's group (Augsburg University). The average size of these nanodiamonds is 100 nm. (a) Overview image, white dots are nanodiamonds. (b) Detail image, it can be seen that not all nanodiamonds exhibit the same size and that they coexist in different shapes.

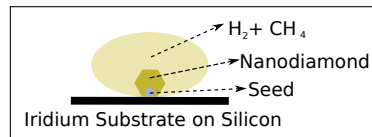


Figure 2.2: Sketch showing the production of CVD nanodiamonds in the growth chamber with a methane gas environment.

rather expensive when compared to the CVD process due to the necessary high temperatures and high pressures.

In the scope of this thesis, HPHT diamonds produced by Davydov et al. [36] are spectroscopically investigated.

## 2.2 Chemical Vapor Deposition Diamond

In contrast to the HPHT process, during the chemical vapor deposition process, diamond is grown from a vapor phase. This process requires moderate temperatures ( $700^{\circ}\text{C}$  to  $1300^{\circ}\text{C}$ ) but low pressures of less than 1 bar in a vacuum chamber [] The diamond in a metastable state Atomic hydrogen is necessary to suppress the simultaneous growth of graphite. The vapor phase within the growth chamber is a mixture of hydrogen and methane, the latter of which acts as a carbon source. Within the vacuum chamber, activation of the gas by an energy source (e.g. microwave plasma) breaks apart the gas molecules to release carbon atoms. These atoms are drawn down toward the cooler substrate. On the substrate surface, various processes occur, such as adsorption, desorption and diffusion. The growth parameters are optimized such that growth of diamond is favored with respect to graphite.

Growth on a substrate is easier, if the lattice constant of the substrate and the crystal to be grown are very similar. The lattice constant of iridium (0.384 nm[37, 38]) is very similar to the lattice constant of diamond (0.356 nm[39]). Therefore, the diamonds were grown on a stratified substrate, consisting of iridium layers of 60 nm to 150 nm thickness grown onto an

sind die  
nicht  
auch zer-  
mahlen  
worden?

wie kom-  
men da  
die SiVs  
rein?

ueberleitu-  
zu naech-  
stem  
satz

yttria-stabilized zirconia (YSZ) buffer layer, which in turn was grown on a silicon wafer [40]. If the lattice constant of the substrate and the diamond are not matched, stress in the diamond lattice is induced. Therefore, the iridium substrate not only facilitates diamond growth, but also reduces unfavorable stress in the nanodiamonds (more on the effect of stress in ??).

For crystals to form in heteroepitactic growth (i.e. one type of crystal is grown upon the surface of a different type), a nucleation step is necessary [41]. The easiest method to obtain nuclei on a substrate is to spin-coat the substrate with small diamond seed crystals of a size of a few nanometers. This method is exploited for all the CVD grown nanodiamonds investigated in this thesis. Such small seed diamond crystals are commercially available, and are usually diamond particles produced by a so-called detonation process. In a detonation process, the high pressure produced by shockwaves of a detonation is used to create very small diamond particles of a size down to a few nanometers. During the CVD growth process, carbon from the methane gas is adsorbed to the seed crystals. To produce nanodiamonds of a desired size, the growth process is stopped when the diamonds grown onto the seed crystals reaches the desired size. If the growth process is continued, the individual crystals grow together to form diamond films. Such diamond films are used as starting material for the wet-milling process described in the next section (Table 2.3)

One of the advantages of the CVD process is that silicon is incorporated *in-situ*. This is achieved by etching of silicon substrate edges by the plasma which automatically occurs in the growth chamber and silicon atoms diffuse into the methane gas. For a higher silicon content in the diamond, sacrificial silicon is put into the growth chamber. These atoms are then built into the diamond lattice while growth.

After nanodiamond growth, the nanodiamonds are either investigated directly on the growth substrate or they are shaken off in an ultrasonic bath to obtain a solution which is coated onto other substrates for further measurements.

In this thesis, two types of samples were investigated which were directly produced as nanodiamonds.<sup>1</sup> The first batch (henceforth called CVD samples) were grown on detonation diamond seeds of a size smaller than 3 nm (produced by the company Microdiamant, product Liquid Diamond monocrystalline, MSY 0-0.03 micron GAF). For the growth process, 1% of methane is added to the hydrogen environment in the growth chamber. The growth process is performed with a pressure of 30 hPa for 30 min to 60 min, yielding nanodiamonds of a diameter of about 100 nm to 200 nm.

The other samples directly produced by a CVD process are nanodiamonds grown onto molecular analogs of diamond crystals. A subgroup of these molecular diamonds are called diamondoids and are carbon crystals based on the carbon cage molecule adamantine  $C_{10}H_{16}$ . The molecular diamonds used for this work are adamantine in cyclohexane, mercapto adamantine in cyclohexane, and cyclohexane. Each of these seed crystals is used in different growth processes. During the growth process, either 3% or 1% methane was added to the hydrogen plasma and either silicon or silicon dioxide was exploited to form *in-situ* incorporated SiV centers (see Table 2.1).

is this  
correct?

irgendwo  
einfue-  
gen, was  
ich dies-  
bezgl.  
gemacht  
hab

put in  
figure

## 2.3 Wet-Milled Nanodiamonds

Apart from growing nanodiamonds of a specific size directly via a CVD process, macroscopic diamond starting material can be crushed to obtain small diamond particles. In contrast

<sup>1</sup>The CVD nanodiamonds were grown by the group of M. Schreck, Augsburg University[].

Table 2.1: Summary of the samples grown on diamondoid seed crystals.

Sample name	Seed crystals	Methane conc.	Silicon source
160211_E	Mercapto adamentane in cyclohexane	1%	SiO <sub>2</sub>
160211_F	Cyclohexane	1%	SiO <sub>2</sub>
160212_C	Cyclohexane	3%	silicon
160212_D	Adamentane in cyclohexane	3%	SiO <sub>2</sub>
160212_E	Mercapto adamentane in cyclohexane	3%	SiOs
160212_F	Cyclohexane	3%	SiO <sub>2</sub>

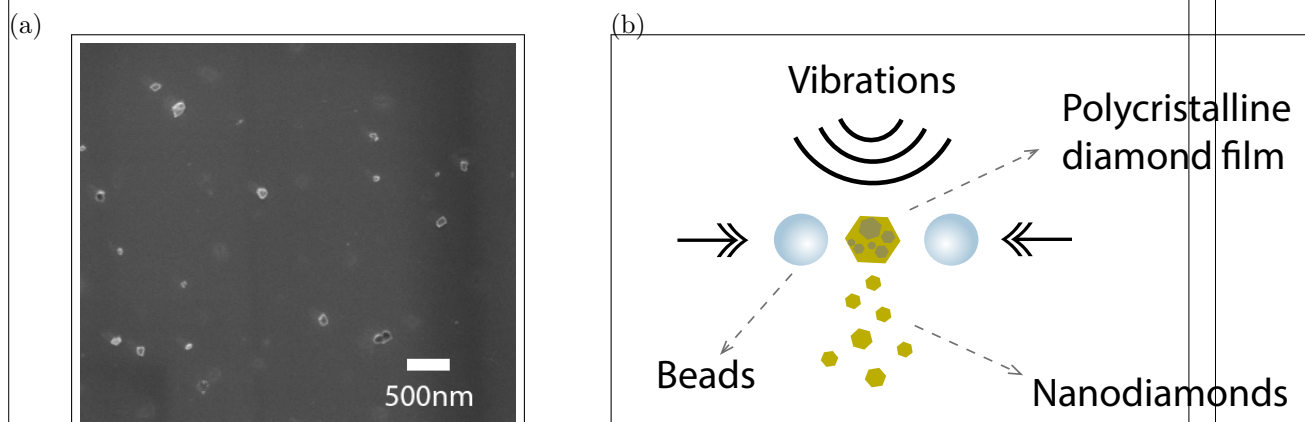


Figure 2.3: Pictures of the milled nanodiamonds (sample insitu100). (a) SEM picture showing the distribution of the nanodiamond crystals on the iridium substrate (sample insitu100). (b) Sketch showing the wet-milling process in a vibrational mill. Vibrations from the mill drive the beads which collide with the diamond material and crush it to smaller pieces.

to nanodiamonds directly grown by a CVD process, the process is divided into two subprocesses: 1. Diamond is produced, for example by an HPHT process or by CVD growth. 2. The macroscopic diamond is milled to smaller diamond particles. For the wet-milling process which yields the nanodiamonds investigated in this thesis<sup>2</sup>, small beads are used to crush the diamond material. The beads are driven by vibrations of a vibrational mill. A sketch of the process is shown in ??.

The big advantage of the milling process is that it enables the production of a large quantity of diamond nanoparticles. When producing nanodiamonds directly via a CVD process, the number of produced nanodiamonds in one process scales with the surface of the substrate on which the nanodiamonds are grown. In contrast, the quantity of milled nanodiamonds scales with the volume of the starting material. Therefore in one and the same process the limit for the obtainable amount of diamond nanoparticles is much higher. Another advantage of the milling process is that the nanodiamonds are in an aqueous solution after milling. Therefore, it is viable to spin-coat the nanodiamonds directly onto any substrate suited for further experiments without further treatment.

The wet-milled nanodiamonds have the disadvantage to contain grain boundaries, resulting in reduced crystal quality (described in more detail in ??). While the polycrystalline diamond film is more likely to break apart at grain boundaries, the final nanodiamonds still contain grain boundaries. In contrast, as-grown CVD nanodiamonds are mainly single crystals.

After milling, the nanodiamonds are treated with post-processing steps including annealing in vacuum and oxidation in air. A detailed description of the processes and their impact is given in ??.

In principle diamond produced by any production method can be used as starting material for the milling process. In the following sections, they are distinguished by the respective starting material and milling method.

### 2.3.1 Wet-Milled HPHT Nanodiamonds

We investigated nanodiamonds, which were produced from a HPHT starting material and milled by a wet-milling process to median sizes of about 45 nm, 80 nm and 260 nm. They were then drop-casted onto an iridium substrate and implanted with  $^{28}\text{Si}^{1+}$ <sup>3</sup>. At last, all HPHT nanodiamonds (samples hphtimp45, hphtimp80, hphtimp260) were oxidized in air at 450°C for 3 h.

### 2.3.2 Wet-Milled chemical vapor deposition Nanodiamonds

In the following paragraphs, details of the production processes of nanodiamond produced by wet-milling a CVD diamond film in a vibrational mill are described. For an overview of the samples refer to Table 2.2. The starting material for the wet-milled nanodiamonds was a nanocrystalline diamond film [42] directly grown on a silicon wafer by CVD. A microwave hydrogen plasma containing 1% methane was used to grow on purified 5 nm nanodiamond seeds

<sup>2</sup>If not otherwise stated, all the mentioned wet-milling processes were carried out by Andreas Muzha in the group of A. Krueger (Julius-Maximilians Universität Würzburg))

<sup>3</sup>Implantation was performed by D. Rogalla, Ruhr-Universität Bochum (RUBION - Zentrale Einrichtung für Ionenstrahlen und Radionuklide)

info  
about vibrational mill

more info

besser formulieren

etwas anders formulieren

implantati parame ters

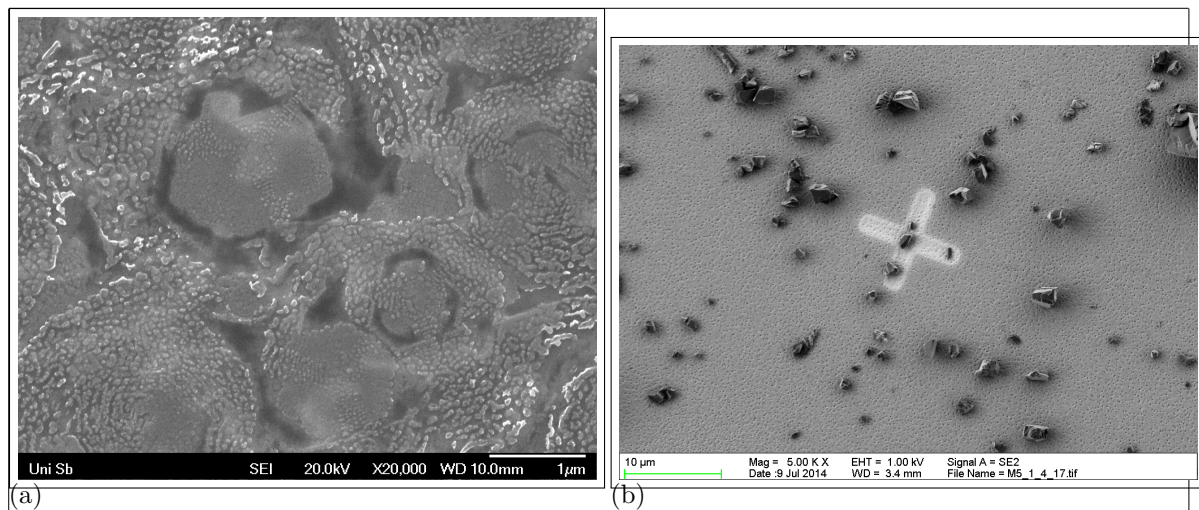


Figure 2.4: (a) SEM picture of nanodiamonds sunken into a silicon substrate after annealing at 900 °C for 3 h. Magnification 20 000. (b) SEM image of the microdiamonds after milling on an iridium substrate, but before implantation. In the middle of the picture, there is a reference cross milled into the iridium substrate with a focused ion beam. Its size amounts to 10  $\mu\text{m}$ . It can be seen, that the microdiamonds exhibit sizes of a few micrometer.

(produced by PlasmaChem). To induce *in-situ* SiV center creation, sacrificial Silicon pieces are situated in the growth chamber. During diamond growth the silicon pieces are etched by the plasma and individual atoms are incorporated into the diamond lattice. The diamond film is then milled by a wet-milling process in a vibrational mill with steel beads. The high amount of steel containment due to the steel beads is removed by extensive acid treatment. We also investigated nanodiamonds milled with silicon nitride beads, and found that the choice of material of the beads does not cause any spectroscopic difference ???. The median diameters of the diamonds are 50 nm, 70 nm and 100 nm (Figure 2.3a). The particle sizes are determined with laser diffraction spectroscopy. Transmission Electron Microscopy (TEM) pictures of the diamond crystals show that the milled nanodiamonds are polycrystalline, exhibiting a typical size of single crystals of a few tens of nanometers. In ?? a TEM image of a typical nanodiamond is shown. Crystal boundaries have effects on the formation of color centers: SiV centers are more prone to form at crystal boundaries [43]. The aqueous solution containing the nanodiamonds is drop cast onto an iridium film on a Silicon substrate. The iridium film of a thickness of 130 nm is grown onto a buffer layer of yttria-stabilized zirconia (YSZ) which in turn is grown onto a Silicon wafer. The iridium surface has the advantage that it acts as an antenna and therefore enhances the collection efficiency of fluorescence light [44] (for more information on the substrate see Table 2.4). Post-procession treatment comprises either both annealing in vacuum at 900 °C and consecutive oxidation in air at a temperature of 450 °C, or only one of the two methods. The duration for either treatment method was 3-6 hours.

### 2.3.3 Doubly Wet-Milled Implanted Nanodiamonds Implanted With Silicon

We also investigated nanodiamonds with SiV centers implanted after diamond growth. Starting material was a polycrystalline Element Six diamond film (electronic grade). In bulk material, the implantation causes the SiV centers to form in a specific depth dependent on the implantation energy, leaving most of the diamond vacant of SiV centers. As a consequence, a big portion of nanodiamonds milled from such a bulk material would not host any SiV centers. To obtain diamond particles with a homogeneous distribution of SiV centers, the process of fabricating implanted nanodiamonds is the following. First, the diamond film is milled to diamond particles of sizes of a few micrometers. In the second step, these microdiamonds are then spin-coated onto iridium substrates and implanted with  $^{28}\text{Si}^{1+}$ . To eliminate lattice damage and vacancies formed by the implantation process, the diamonds were annealed in vacuum and subsequently oxidized. At last, the micrometer sized diamond particles are milled to smaller sizes.

#### Preliminary Tests

The starting material was an Element Six electronic grade diamond film. The diamond was milled in a wet-milling process to sizes on the order of micrometers, which were then coated onto a silicon substrate. The microdiamonds were implanted with  $^{28}\text{Si}^{1+}$  at an implantation energy of 1.7 MeV, and fluences of  $10^9 \text{ cm}^{-2}$  to  $10^{12} \text{ cm}^{-2}$ <sup>4</sup>. After implantation, the microdiamonds on the silicon substrate were annealed for 2 h at 900 °C and oxidized in air for another 2 h at 450 °C. However, we encountered the problem that the silicon sublimated and re-nucleated during annealing, causing the diamonds to sink into the silicon surface (Figure 2.4a). Iridium is less prone to damage by high temperatures and withstands annealing procedures up to our standard annealing temperature of 900 °C without problems. Therefore, we used a sample with microdiamonds on a silicon substrate which was not annealed to shake the nanodiamonds off the silicon substrate in an ultrasonic bath, and consecutively coated the microdiamonds on an iridium substrate. After annealing and oxidizing the nanodiamonds on the iridium substrate, the iridium surface was intact.

#### Final Procedure

For the milling process in a vibrational mill, a minimum amount of diamond material is necessary. When starting with a diamond film, this threshold is easily reached, however, a big quantity of microdiamonds is needed to meet the requirements. Therefore, production was carried out at a larger scale after the preliminary tests. The microdiamonds were directly spin-coated onto iridium substrates, implanted with  $^{28}\text{Si}^{1+}$  (implantation energy 900 keV, fluence  $10^{11} \text{ cm}^{-2}$ )<sup>5</sup>. The microdiamonds were then annealed in vacuum for 3 h at 900 °C and oxidized in air for 3 h at 450 °C. At last, they were milled again to sizes of about 40 nm, 45 nm, 240 nm and 260 nm. The diamonds of sizes 40 nm and 240 nm were annealed in vacuum at 1200 °C.

<sup>4</sup>Implantation performed by D. Rogalla, Ruhr-Universität Bochum (RUBION - Zentrale Einrichtung für Ionenstrahlen und Radionuklide).

<sup>5</sup>Implantation performed by J. Klug at rubitec - Gesellschaft für Innovation und Technologie der Ruhr-Universität Bochum mbH.

how  
much?

time?

Table 2.2: Summary of the wet-milled samples. The first column indicates the names of the samples, the second the mean diameter of the nanodiamonds, and the third describes how the silicon was incorporated into the diamond.

Sample name	Size	Si incorporation	Post-processing
hphtimp45	45 nm	<i>implanted</i>	oxidized in air at 450 °C
hphtimp80	80 nm	<i>in-situ</i>	annealed in vacuum for 1 h at 1000 °C and at 900 °C for 3 h
hphtimp260	260 nm	<i>in-situ</i>	oxidized in air at 450 °C
insitu50	50 nm	<i>in-situ</i>	series of individual samples with diverse post-processing steps
insitu70	70 nm	<i>in-situ</i>	series of individual samples with diverse post-processing steps
insitu70n	70 nm	<i>in-situ</i>	no post-processing subset of insitu70
insitu70o	70 nm	<i>in-situ</i>	oxidized in air at 450 °C subset of insitu70
insitu100	100 nm	<i>in-situ</i>	series of individual samples with diverse post-processing steps
insitu100ao	100 nm	<i>in-situ</i>	annealed in vacuum at 900 °C, consecutively oxidized in air at 450 °C subset of insitu100
implanted250ao	250 nm	implanted	annealed in vacuum at 900 °C, consecutively oxidized in air at 450 °C
hphtimp260	40 nm	implanted	annealed in vacuum at 1200 °C, consecutively oxidized in air at 450 °C
hphtimp260	50 nm	implanted	oxidized in air at 450 °C
hphtimp260	240 nm	implanted	annealed in vacuum at 1200 °C, consecutively oxidized in air at 450 °C
hphtimp260	260 nm	implanted	oxidized in air at 450 °C

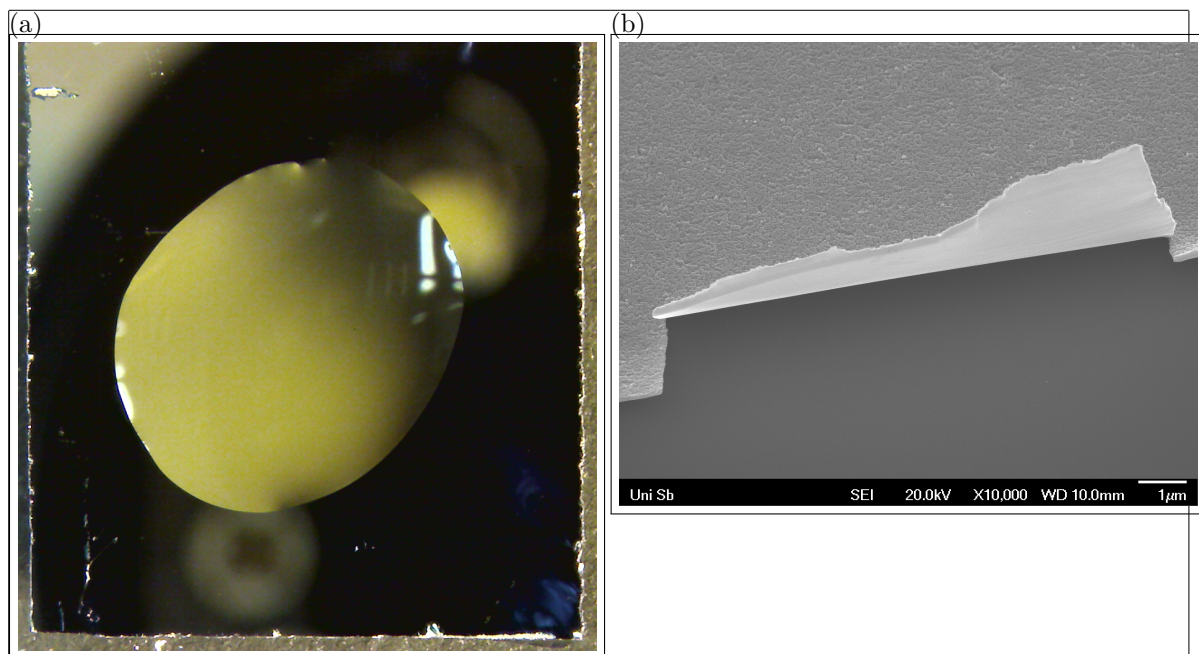


Figure 2.5: (a) Microscope image of a drop of water on an iridium substrate cleaned with Piranha etch. This picture was used to estimate the contact angle. (b) SEM picture of an 60 nm iridium layer that peeled off the substrate after an ultrasonic bath.

## 2.4 Iridium Substrate

As mentioned in section 2.2, we used a silicon substrate with an iridium layer on top for most experiments in order to match the lattice constant of diamond. We also use the same substrates for the experiments with wet-milled diamonds, as the iridium exhibits further advantages:

- The high hydrophilicity of iridium enhances the homogeneity of the nanodiamonds on the substrate after spin-coating or drop-casting. The hydrophilicity is further improved by treating the substrate in a Piranha etch (50:50 mixture of sulfuric acid  $H_2SO_4$  and hydrogen peroxide  $H_2O_2$ ) by removing oxide layers on the surface. The treatment with Piranha etch also has the advantage that all organic contamination is removed. Measurements after applying the Piranha cleaning yielded an estimation of the contact angle of slightly more than one degree. To determine the contact angle with water, the volume of a water drop is compared to the surface it covers after dropping it onto an iridium substrate. From that an estimation of the contact angle is deduced.
- During the post-processing steps, it is of major importance, that the substrate can withstand high temperatures. As described in section 2.3.3 during the preliminary tests with implanted nanodiamonds on a silicon substrate (sample name ), we encountered difficulties with diamonds on a silicon substrate as they sunk into the surface after annealing. In contrast, iridium withstands the used annealing process without damage.
- Additionally to the mentioned technical advantages, another advantage of the iridium surface manifests itself during spectroscopic measurements: Iridium acts both as a mirror and as an antenna for the fluorescence light emitted by the SiV center [44].

check  
numbers

sample  
name

Therefore, the collection efficiency of the fluorescence light is enhanced.

These advantages of iridium surfaces are only countered by one minor disadvantage: If the iridium layer is too thin, it tends to peel off the substrate (Figure 2.5b). We encountered this problem during a cleaning procedure in the ultrasonic bath. However, this disadvantage is easily circumvented by using a thicker iridium layer. For our measurements, we used an iridium layer of a thickness of 130 nm, with which we did not encounter any adhesion problems.

#### 2.4.1 Preparation of The Substrate

Prior to drop casting, the substrate is cleaned. The standard cleaning procedure comprised the following cleaning steps in an ultrasonic bath (3 min to 7 min each):

- Distilled water with a drop of dishwasher detergent
- Isopropanol (99.9% p.a.)
- Acetone (99.9% p.a.)
- Distilled water

Thereafter, the substrates are put into a Piranha solution (50% sulfuric acid  $H_2SO_4$ , 50% hydrogen peroxide  $H_2O_2$ ) to enhance the surface hydrophilicity and therefore obtain a homogeneous distribution of diamonds on the surface. They are then put again into distilled water and blown dry with compressed air to avoid residue from the water. The substrates were then either drop-casted or spin-coated with aqueous diamond solutions. For the prior, the substrates are heated to a temperature of 60 °C and drops of a volume of about 5  $\mu L$  dropped onto the substrate. If substantially more than 5  $\mu L$  is needed, the several drops of about 5  $\mu L$  are dropped onto the substrate consecutively, as with a single big drop the solution would flow off the substrate before drying. For spin-coating, a home built spin coater was used. Drops of 5  $\mu L$  are dropped on the substrate and the spin-coater set to a velocity of 2500 rpm for 3 min.

# Bibliography

- [1] Elke Katja Neu. *Silicon vacancy color centers in chemical vapor deposition diamond : new insights into promising solid state single photon sources*. PhD thesis, 2012. 1, 2, 5, 9
- [2] David Steinmetz. Ni / Si-basierte Farbzentren in Diamant als Einzelphotonenquellen Dissertation. 2011. 1, 4
- [3] F. P. Bundy. Pressure-temperature phase diagram of elemental carbon. *Physica A: Statistical Mechanics and its Applications*, 156(1):169–178, 1989. 1
- [4] Takao Saotome, Kazutoshi Ohashi, Toshimaro Sato, Hiroshi Maeta, Katsuji Haruna, and Fumihsisa Ono. Thermal expansion of a boron-doped diamond single crystal at low temperatures. *Journal of Physics: Condensed Matter*, 10(6):1267–1272, feb 1998. 1
- [5] C. D. Clark, P. J. Dean, and P. V. Harris. Intrinsic Edge Absorption in Diamond. *Proceedings of the Royal Society A: Mathematical, Physical and Engineering Sciences*, 277(1370):312–329, feb 1964. 1
- [6] W. Saslow, T. K. Bergstresse, and Marvin L. Cohen. Band structure and optical properties of diamond. *Physical review letters*, 16(9):354–356, 1966. 1
- [7] Richard P. Mildren, James E. Butler, and James R. Rabeau. CVD-diamond external cavity Raman laser at 573 nm. *Optics Express*, 16(23):18950, 2008. 1
- [8] AM Zaitsev. *Optical properties of diamond: a data handbook*. 2001. 2, 3, 4
- [9] Alexios Beveratos, Rosa Brouri, Thierry Gacoin, Jean-Philippe Poizat, and Philippe Grangier. Nonclassical radiation from diamond nanocrystals. *Physical Review A*, 64(6):61802, nov 2001. 2
- [10] John Walker and John Walkert. Optical absorption and luminescence in diamond. *Rep. Prog. Phys.*, 42:1606–1659, 1979. 3
- [11] B. Massarani, J. C. Bourgoin, and R. M. Chrenko. Hopping conduction in semiconducting diamond. *Physical Review B*, 17(4):1758–1769, feb 1978. 3
- [12] M. L. Markham, J. M. Dodson, G. A. Scarsbrook, D. J. Twitchen, G. Balasubramanian, F. Jelezko, and J. Wrachtrup. CVD diamond for spintronics. *Diamond and Related Materials*, 20(2):134–139, 2011. 3
- [13] Gopalakrishnan Balasubramanian, Philipp Neumann, Daniel Twitchen, Matthew Markham, Roman Kolesov, Norikazu Mizuuchi, Junichi Isoya, Jocelyn Achard, Johannes Beck, Julia Tissler, Vincent Jacques, Philip R. Hemmer, Fedor Jelezko, and Jörg

- Wrachtrup. Ultralong spin coherence time in isotopically engineered diamond. *Nature Materials*, 8(5):383–387, 2009. 3
- [14] P. W. May. Diamond thin films: a 21st-century material. *Philosophical Transactions of the Royal Society A: Mathematical, Physical and Engineering Sciences*, 358(1766):473–495, jan 2000. 3
- [15] Axel Kuhn, Markus Hennrich, and Gerhard Rempe. Deterministic Single-Photon Source for Distributed Quantum Networking. *Physical Review Letters*, 89(6):4–7, 2002. 4
- [16] Matthias Keller, Birgit Lange, Kazuhiro Hayasaka, Wolfgang Lange, and Herbert Walther. Continuous generation of single photons with controlled waveform in an ion-trap cavity system. *Nature*, 431(7012):1075–1078, oct 2004. 4
- [17] P Michler, A Kiraz, C Becher, W V Schoenfeld, P M Petroff, L Zhang, E Hu, and A Imamoglu. A quantum dot single-photon turnstile device. *Science (New York, N.Y.)*, 290(5500):2282–5, dec 2000. 4
- [18] Zhiliang Yuan, Beata E Kardynal, R Mark Stevenson, Andrew J Shields, Charlene J Lobo, Ken Cooper, Neil S Beattie, David A Ritchie, and Michael Pepper. Electrically driven single-photon source. *Science (New York, N.Y.)*, 295(5552):102–5, jan 2002. 4, 8
- [19] Brahim Lounis and Michel Orrit. Single-photon sources. *Reports on Progress in Physics*, 68(5):1129–1179, may 2005. 4
- [20] T. A. Kennedy, J. S. Colton, J. E. Butler, R. C. Linares, and P. J. Doering. Long coherence times at 300 K for nitrogen-vacancy center spins in diamond grown by chemical vapor deposition. *Applied Physics Letters*, 83(20):4190–4192, nov 2003. 4
- [21] K. Iakoubovskii and G.J. Adriaenssens. Optical detection of defect centers in CVD diamond. *Diamond and Related Materials*, 9(7):1349–1356, 2000. 6
- [22] M. C. Rossi, S. Salvatori, F. Galluzzi, R. M. Montereali, and F. Somma. Emission and excitation spectra of silicon-related luminescent centers in CVD-grown diamond films. *Diamond and Related Materials*, 6(10):1564–1567, 1997. 6
- [23] T. Müller, I. Aharonovich, L. Lombez, Y. Alaverdyan, A. N. Vamivakas, S. Castelletto, F. Jelezko, J. Wrachtrup, S. Prawer, and M. Atatüre. Wide-range electrical tunability of single-photon emission from chromium-based colour centres in diamond. *New Journal of Physics*, 13, 2011. 6
- [24] P. Siyushev, V. Jacques, I. Aharonovich, F. Kaiser, T. Müller, L. Lombez, M. Atatüre, S. Castelletto, S. Prawer, F. Jelezko, and J. Wrachtrup. Low-temperature optical characterization of a near-infrared single-photon emitter in nanodiamonds. *New Journal of Physics*, 11, 2009. 6
- [25] G. Davies. The Jahn-Teller effect and vibronic coupling at deep levels in diamond. *Reports on Progress in Physics*, 44(7):787–830, jul 1981. 6, 9
- [26] A. M. Zaitsev. Vibronic spectra of impurity-related optical centers in diamond. *Physical Review B*, 61(19):12909–12922, may 2000. 6, 9
- [27] J. L. Dugall, M. S. Godfrey, K. A. Harrison, W. J. Munro, and J. G. Rarity. Low cost and compact quantum key distribution. *New Journal of Physics*, 8, 2006. 8

- [28] Maximilian Nothaft, Steffen Höhla, Fedor Jelezko, Norbert Fröhlauf, Jens Pflaum, and Jörg Wrachtrup. Electrically driven photon antibunching from a single molecule at room temperature. *Nature Communications*, 3, 2012. 8
- [29] Tom Feng and Bradley D. Schwartz. Characteristics and origin of the 1.681~{eV} luminescence center in chemical-vapor-deposited diamond films. *J. Appl. Phys.*, 73(3):1415, feb 1993. 9
- [30] S. A. Solin and A. K. Ramdas. Raman Spectrum of Diamond. *Physical Review B*, 1(4):1687–1698, feb 1970. 9
- [31] M. H. Grimsditch, E. Anastassakis, and M. Cardona. Effect of uniaxial stress on the zone-center optical phonon of diamond. *Physical Review B*, 18(2):901–904, 1978. 9
- [32] H. Sternschulte, K. Thonke, R. Sauer, P. C. Münzinger, and P. Michler. 1.681-eV luminescence center in chemical-vapor-deposited homoepitaxial diamond films. *Physical Review B*, 50(19):14554–14560, nov 1994. 9
- [33] B. Huttner, N. Imoto, N. Gisin, and T. Mor. Quantum cryptography with coherent states. *Physical Review A*, 51(3):1863–1869, 1995. 9
- [34] R F Davis. *Diamond Films and Coatings: Development, Properties, and Applications*. Hébert, Alexandre-Martin-Stanislas. Noyes Pub., 1993. 11
- [35] K H O'Donovan. Synthetic diamond. 11
- [36] Valery a. Davydov, a. V. Rakhmanina, S. G. Lyapin, I. D. Il'ichev, K. N. Boldyrev, a. a. Shiryaev, and Viatcheslav N. Agafonov. Production of nano- and microdiamonds with Si-V and N-V luminescent centers at high pressures in systems based on mixtures of hydrocarbon and fluorocarbon compounds. *JETP Letters*, 99(10):585–589, 2014. 12
- [37] John W. Arblaster. Crystallographic Properties of Iridium. *Platinum Metals Review*, 54(2):93–102, 2010. 12
- [38] S. Gsell, M. Fischer, R. Brescia, M. Schreck, P. Huber, F. Bayer, B. Stritzker, and D. G. Schlom. Reduction of mosaic spread using iridium interlayers: A route to improved oxide heteroepitaxy on silicon. *Applied Physics Letters*, 91(6):061501, aug 2007. 12
- [39] Robert F. Davis, editor. *Diamond Films and Coatings*. Noyes Pub., 1993. 12
- [40] S. Gsell, T. Bauer, J. Goldfuß, M. Schreck, and B. Stritzker. A route to diamond wafers by epitaxial deposition on silicon via iridium/yttria-stabilized zirconia buffer layers. *Applied Physics Letters*, 84(22):4541, may 2004. 13
- [41] Matthias Schreck, Jes Asmussen, Shinichi Shikata, Jean-Charles Arnault, and Naoji Fujimori. Large-area high-quality single crystal diamond. *MRS Bulletin*, 39(06):504–510, jun 2014. 13
- [42] Oliver A. Williams and Milos Nesládek. Growth and properties of nanocrystalline diamond films. *Phys. status solidi*, 203(13):3375–3386, oct 2006. 15
- [43] Peter Zapol, Michael Sternberg, Larry Curtiss, Thomas Frauenheim, and Dieter Gruen. Tight-binding molecular-dynamics simulation of impurities in ultrananocrystalline diamond grain boundaries. *Physical Review B*, 65(4):045403, 2001. 16

- [44] Elke Neu, Mario Agio, and Christoph Becher. Photophysics of single silicon vacancy centers in diamond: implications for single photon emission. *Optics Express*, 20:19956–19971, jul 2012. 16, 19